An essential role for the Zn2+ transporter ZIP7 in B cell development

Consuelo Anzilotti[1], **David J. Swan**[2,§], **Bertrand Boisson**[3,4,5,§], **Mukta Deobagkar-Lele**[1], **Cathy Oliveira**[6], **Pauline Chabosseau**[7], **Karin R Engelhardt**[2], **Xijin Xu**[1], **Rui Chen**[2], **Luis Alvarez**[6], **Rolando Berlinguer-Palmini**[8], **Katherine R. Bull**[1], **Eleanor Cawthorne**[1], **Adam P. Cribbs**[9], **Tanya L. Crockford**[1], **Tarana Singh Dang**[2], **Amy Fearn**[10], **Emma J. Fenech**[11], **Sarah J. de Jong**[3], **B. Christoffer Lagerholm**[1], **Cindy S. Ma**[12,13], **David Sims**[9], **Bert van den Berg**[10], **Yaobo Xu**[14], **Andrew J. Cant**[15], **Gary Kleiner**[16], **T. Ronan Leahy**[17], **M. Teresa de la Morena**[18], **Jennifer M. Puck**[19,20], **Ralph S. Shapiro**[21], **Mirjam van der Burg**[22], **J. Ross Chapman**[6], **John C. Christianson**[11], **Ben Davies**[6], **John A. McGrath**[23], **Stefan Przyborski**[24], **Mauro Santibanez Koref**[14], **Stuart G. Tangye**[12,13], **Andreas Werner**[10], **Guy A. Rutter**[7], **Sergi Padilla-Parra**[6,25,26], **Jean-Laurent Casanova**[3,4,5,27,28], **Richard J. Cornall**[1,*], **Mary Ellen Conley**[3,*], and **Sophie Hambleton**[2,15,*]

[1]MRC Human Immunology Unit, Weatherall Institute of Molecular Medicine, University of Oxford, Oxford, UK [2]Primary Immunodeficiency Group, Institute of Cellular Medicine, Newcastle University, Newcastle upon Tyne, UK [3]St Giles Laboratory of Human Genetics of Infectious Diseases, Rockefeller Branch, The Rockefeller University, New York, NY, USA [4]Laboratory of Human Genetics of Infectious Diseases, Necker Branch, Inserm U1163 Necker Hospital for Sick Children, Paris, France, EU [5]Paris Descartes University, Imagine Institute, Paris, France, EU [6]Wellcome Centre for Human Genetics, University of Oxford, Oxford, UK [7]Section of Cell Biology and Functional Genomics, Division of Diabetes, Endocrinology and Metabolism, Department of Medicine, Imperial College, London, UK [8]Bioimaging Unit, Newcastle University Medical School, Newcastle upon Tyne, UK [9]MRC WIMM Centre for Computational Biology, Weatherall Institute of Molecular Medicine, University of Oxford, Oxford, UK [10]Institute for Cell and Molecular Biosciences, Newcastle University, Newcastle upon Tyne, UK [11]Ludwig Institute for Cancer

Research, University of Oxford, Oxford, UK [12.]Garvan Institute of Medical Research, Darlinghurst, NSW, Australia [13.]St Vincent's Clinical School, Faculty of Medicine, University of NSW, Darlinghurst, NSW, Australia [14.]Institute of Genetic Medicine, Newcastle University, Newcastle upon Tyne, UK [15.]Great North Children's Hospital, Newcastle upon Tyne Hospitals NHS Foundation Trust, Newcastle upon Tyne, UK [16.]Pediatric Allergy and Immunology, University of Miami Miller School of Medicine, Miami FL, USA [17.]Paediatric Immunology and Infectious Diseases, Our Lady's Children's Hospital, Crumlin, Dublin, Ireland [18.]Division of Immunology, Department of Pediatrics, University of Washington and Seattle Children's Hospital, Seattle, WA, USA [19.]Department of Pediatrics, Division of Allergy, Immunology, and Blood and Bone Marrow Transplantation, University of California San Francisco, USA [20.]UCSF Benioff Children's Hospital, San Francisco, CA, USA [21.]Midwest Immunology Clinic, Plymouth, MN, USA [22.]Department of Immunology, Erasmus University Medical Centre, Rotterdam, Netherlands [23.]St John's Institute of Dermatology, King's College London, London, UK [24.]Department of Biosciences, Durham University, Durham, UK [25.]Dynamic Structural Virology Group, Biocruces Health Research Institute, Barakaldo, Spain [26.]Ikerbasque, Basque Foundation for Science, Bilbao, Spain [27.]Pediatric Hematology-Immunology Unit, Necker Hospital for Sick Children, Paris, France [28.]Howard Hughes Medical Institute, New York, NY, USA

Abstract

Despite the known importance of zinc for human immunity, molecular insights into its roles have remained limited. Here we report a novel autosomal recessive disease characterized by absent B cells, agammaglobulinemia and early-onset infections in five unrelated families. The immunodeficiency results from hypomorphic mutations of *SLC39A7*, which encodes the endoplasmic reticulum–to–cytoplasm zinc transporter ZIP7. Using CRISPR-Cas9 mutagenesis we have precisely modelled ZIP7 deficiency in mice. Homozygosity for a null allele caused embryonic death, but hypomorphic alleles reproduced the block in B cell development seen in patients. B cells from mutant mice exhibited a diminished concentration of cytoplasmic free zinc, increased phosphatase activity and decreased phosphorylation of signalling molecules downstream of the pre-B cell and B cell receptors. Our findings highlight a specific role for cytosolic Zn^{2+} in modulating B cell receptor signal strength and positive selection.

The molecular dissection of primary immunodeficiencies is a powerful means of elucidating genes and pathways critical for immune function. In the case of B cell development, linkage analysis and subtractive hybridization in boys with X-linked agammaglobulinemia (XLA) led to the discovery of the first B cell immunodeficiency disease gene, Bruton's Tyrosine Kinase (*BTK*)[1, 2]. This kinase is now the target of drugs effective in treating numerous B cell malignancies[3]. Although its expression is not confined to the B cell lineage, it is in B cells that BTK performs its major non-redundant function as a signalling molecule downstream of the nascent pre-B and B cell receptors (BCR).

B cells must rearrange first heavy and then light chain immunoglobulin (Ig) genes as they proceed through an orderly programme of development, and pass corresponding quality control checkpoints that signal the expression of first the pre-BCR and then the BCR

respectively. Confirming the importance for developing human B cells of survival signals emanating from the pre-BCR/BCR, autosomal recessive causes of B cell deficiency have been identified within the antigen receptor itself (*IGHM, IGLL1*), its signalling adaptors (*CD79A, CD79B*) and other downstream signal transducers (*BLNK, PIK3R1*). Together with *BTK*, these defects of pre-BCR and BCR signalling account for the vast majority of early onset agammaglobulinemias, and few patients remain without a molecular diagnosis in the USA and Europe[4-6].

The divalent cations, Ca^{2+} and Mg^{2+}, are well established as mediators of lymphocyte cell signalling and inherited deficiency in their transmembrane transporters (*ORAI1*[7] and *MAGT1*[8]) causes a combined B and T cell immunodeficiency and a T or NK cell immunodeficiency respectively. A third divalent cation, Zn^{2+}, contributes to the structural and functional integrity of over 3,000 proteins, and is tightly regulated by buffering and by 14 *SLC39A* (ZIP) and 10 *SLC30A* (ZnT) Zn^{2+} transporters, which control the movement of Zn^{2+} between the cytosol and the extracellular space or cytoplasmic organelles[9]. Dietary zinc deficiency causes lymphopenia[10] and loss of ZIP10 has also been associated with B cell immunodeficiency in mice[11]; however, the mechanism(s) by which Zn^{2+} might regulate lymphocyte development in humans are not established. The MHC region of human chromosome 6, which is highly enriched for immunologically relevant genes, includes a single Zn^{2+} transporter, originally termed "Really Interesting New Gene 5" or *HKE4* but now known as *SLC39A7*. No immunological function has previously been ascribed to this gene. Here we report a novel human immunodeficiency syndrome caused by multiple loss of function alleles in *SLC39A7* (ZIP7), which lead to reduced B cell signalling at the positive selection checkpoints.

Results

A novel human immunodeficiency syndrome

We used whole exome sequencing to investigate patients with early onset agammaglobulinemia and absent B cells of unknown cause, and sought candidate autosomal recessive disease genes bearing rare biallelic variants. Six individuals from 5 kindreds of white European, South Asian or Hispanic ancestry, were found to harbor compound heterozygous (4 families) or homozygous (1 family) rare variants in *SLC39A7* (Fig. 1a). This gene, not previously linked to the immune system other than by its location within the MHC complex on chromosome 6, encodes ZIP7, a ubiquitously expressed channel protein that regulates Zn^{2+} egress from the endoplasmic reticulum (ER) into the cytoplasm[12]. Consistent with a causal link to a rare autosomal recessive disease, population data[13] revealed that none of the patients' variants of *SLC39A7*, nor any predicted null (nonsense/frameshift/essential splice-site) alleles, occurs with a frequency of greater than 1/1,000 (Supplementary Fig. 1) and none has previously been found in a homozygous state. In general, patients' ethnicity matched that of the population in which the corresponding *SLC39A7* variant(s) had been reported; two missense alleles each occurred in two independent kindreds of European ancestry. The five missense and two nonsense variants were all predicted to be deleterious (CADD score 25)[14] (Supplementary Fig. 1).

Affected individuals presented with early onset infections, agammaglobulinemia and absence of circulating B cells but normal T cell numbers and proliferative responses (Table 1 and Supplementary Table 1). Naïve T cells were abundant, in keeping with age, while effector and memory subsets were correspondingly reduced but not absent. The two most severely affected children (P1 and P2, family 1) additionally showed severe blistering dermatosis (Fig. 1b), failure to thrive and thrombocytopenia, prompting hematopoietic stem cell transplantation; this resulted in cure of immunologic abnormalities and amelioration of skin disease. Other patients have generally responded well to Ig replacement therapy alone, although P4 has suboptimal growth, enteropathy and liver dysfunction while P5 has seborrheic dermatitis. Family members who were heterozygous for a wild type (WT) and a mutant allele demonstrated normal immune function. Bone marrow (BM) examination in P1 and P2 showed a progressive failure of B cell development with an excess of pro-B cells relative to pre-B cells, and an even lower proportion of immature B cells relative to pre-B cells, similar to that seen in XLA caused by mutations in *BTK* (Fig. 1c)[4].

To explore the impact of disease-associated mutations, we first examined ZIP7 protein expression by immunoblotting and immunofluorescence microscopy in primary patient fibroblasts (Fig. 2a and Supplementary Fig. 2a), and transfected cell lines (Fig. 2b-e). Similar to endogenous WT ZIP7 (Fig. 2c), each variant was expressed and predominantly localized to the ER of transfected cells (Fig. 2d, e), although the protein products of nonsense variants were truncated when visualized on SDS-PAGE (Fig. 2b). The detrimental effects of missense amino acid substitutions were illuminated by modelling into the predicted multi-pass membrane channel structure of human ZIP7, based on alignment with a recently solved bacterial ZIP (BpZIP; 26% sequence identity)(Fig. 2f, g and Supplementary Fig 1c)[15]. In most cases, the amino acid change (P190A, L217P, G458A) involves either a glycine or proline, residues that are often conserved and known to be critical for membrane protein structure. In the case of P190A and L217P, the removal and introduction of a proline, respectively, is likely to affect the conformation and/or dynamics of their respective helices, and perhaps that of the intervening, histidine-rich cytoplasmic loop. The G458A change will disrupt packing interactions of helices H8 and H2 in the protein interior, which, with H2 lining the active site, is likely to disrupt function. Of the remaining two mutations, T395I is at first sight enigmatic, because it corresponds to a semi-conservative change of a lipid-exposed residue. However, this most likely reflects an alignment gap; once both H6 helices are aligned, the Thr395 corresponds to Glu240 in BpZIP (or an adjacent residue), one of the active site residues coordinating Zn^{2+} within the channel. The effect of the final E363K mutation is very clear, as this will place a positively charged side chain in or near this active site (Fig. 2f and g).

These analyses strongly implied that disease alleles were either null or hypomorphic with respect to Zn^{2+} transport function. To test this hypothesis, we compared the function of P190A and E363K missense mutants, which were co-expressed in the most severely affected family 1, with WT ZIP7, by injecting mRNA transcripts into *Xenopus* oocytes and visualizing Zn^{2+} ingress by means of a Zn^{2+}-sensitive dye (Fig. 2h and Supplementary Fig. 2b, c). In keeping with hypomorphic behavior, the Zn^{2+} signal generated by either mutant ZIP7 was significantly reduced compared with WT (Fig. 2h), despite similar amounts of protein expression (Supplementary Fig. 2c). Similar data were obtained in mammalian cells

transfected with a eCALWY-4 Fluorescence Energy Transfer (FRET) probe for cytoplasmic Zn^{2+} alongside WT or mutant ZIP7 (Supplementary Fig. 2d and e)[16]. Taken together, these studies imply residual ZIP7 protein expression but reduced function in patients bearing pathogenic mutations.

Mouse ZIP7 hypomorphs model human disease

To model the human disease, we used CRISPR-Cas9 genome editing[17] to generate C56BL/6J (B6) mice carrying a ZIP7 P198A mutation, orthologous to the most N terminal human P190A mutation found in 2 independent kindreds. We chose a knock-in rather than a knockout approach because we suspected complete loss of function would be embryonic lethal. The error-prone non-homologous end-joining repair pathway nonetheless generated a series of different ZIP7 alleles in mouse zygotes, which allowed us to investigate a range of phenotypes. These variants included *null* alleles due to frameshift mutations, the P198A mutation itself, and an insertional mutant H199QV, which was also expressed at the protein level (Fig. 3a).

Mice with homozygous ($ZIP7^{P198A/P198A}$ or $ZIP7^{H199QV/H199QV}$) or compound heterozygous ($ZIP7^{P198A/H199QV}$) hypomorphic mutations demonstrated profound B cell immunodeficiency (Fig. 3b), whereas heterozygous mice with wild-type alleles had normal B cell numbers. Other effects of the ZIP7 mutations on growth and skin varied by allele, with severity ranging from WT < H199QV < P198A < null. Homozygous $ZIP7^{H199QV/H199QV}$ and compound heterozygous $ZIP7^{P198A/H199QV}$ mice showed mild weight restriction compared with WT, whereas $ZIP7^{P198A/P198A}$ mice were growth retarded with mottled gray fur, and few of these animals survived beyond 6 weeks (Fig. 3c and d). $ZIP7^{-/-}$, $ZIP7^{-/P198A}$ and $ZIP7^{-/H199QV}$ mice carrying the *null* allele could not be obtained. These findings are consistent with an absolute requirement for some residual ZIP7 function during embryonic development, albeit less than that required for developing B cells. The murine ZIP7 mutations therefore lead to quantitative traits affecting the skin and growth, and a qualitative trait affecting B cell development (Fig 3e).

To investigate the role of ZIP7 in B cell development, we focused on mice homozygous for the hypomorphic P198A allele, mimicking one of the human disease variants. Comparison of 25-day-old WT and $ZIP7^{P198A/P198A}$ mice showed strikingly reduced numbers of $B220^{+}CD43^{-}IgM^{-}IgD^{-}$ late pre-B cells (Hardy fraction (Fr) D), $B220^{+}CD43^{-}IgM^{+}IgD^{-}$ immature B cells (FrE) and recirculating $B220^{+}CD43^{-}IgM^{+}IgD^{+}$ mature B cells (FrF) in the ZIP7-deficient BM (Fig. 4a and b)[18]. Peripheral B cell numbers were further reduced in the spleen with progressive loss from $CD93^{+}IgM^{hi}CD23^{-}$ transitional T1 to $CD93^{+}IgM^{hi}CD23^{+}$ T2, $CD93^{+}IgM^{+}CD23^{+}$ T3, $CD93^{-}IgM^{+}IgD^{+}CD23^{+}CD21^{+}$ follicular and $CD93^{-}IgM^{hi}IgD^{-}CD23^{-}CD21^{hi}$ marginal zone B cells (Fig. 4a and b). To compare absolute numbers of developing B cell subsets independently of the small size of $ZIP7^{P198A/P198A}$ mice, we reconstituted lethally irradiated $CD45.1^{+}$ WT mice for 8 weeks with WT or $ZIP7^{P198A/P198A}CD45.2^{+}$ BM and repeated our analysis. This confirmed a highly significant reduction in developing B cell numbers, which was most evident in Hardy FrD and FrE (Fig 4c). There was no rescue of B cell development in BM chimeric mice fed 0.5mM $ZnSO_4.7H_2O$ in drinking water for the 8 weeks period of reconstitution: 0.73×10^6 (95% CI

0.71-0.74 $\times$ 10^6, n=4) and 0.79 $\times$ 10^6 (0.76-0.81 $\times$ 10^6, n=4) splenic follicular B cells respectively in untreated and treated ZIP7$^{P198A/P198A}$ mice, compared to 85.9 $\times$ 10^6 (85.6-86.1 $\times$ 10^6, n=5) and 85.4 $\times$ 10^6 (85.03-85.9 $\times$ 10^6, n=5) respectively in WT mice.

B cells constituted only 0.76% (0.76-0.77%, 95% CI) of total blood lymphocytes in 4-week-old ZIP7$^{P198A/P198A}$ mice, compared to 27.96% (27.71-28.21%, 95% CI) in age-matched WT controls; and serum IgM antibody concentrations in 4-6 week ZIP7$^{P198A/P198A}$ and WT mice were 104 μg/ml (103-106 μg/ml, 95% CI) and 383 μg/ml (378-388 μg/ml, 95% CI) respectively. Because ZIP7$^{P198A/P198A}$ mice rarely survived long after weaning, endogenous IgG production could not be assessed. However, mice of the milder hypomorphic genotype ZIP7$^{P198A/H199QV}$ showed a dramatic decline in IgG concentrations beyond this age (146-150 μg/ml, 95% CI, compared to 1830-1870 μg/ml, 95% CI, in WT mice, aged 7-13 weeks). T cell development and peripheral T cell numbers were normal, as were other leukocyte populations (Supplementary Fig. 3). These data thus confirmed a selective and profound failure of B cell development in ZIP7-mutated mice.

Developmental arrest in ZIP7-deficient B cells

To distinguish between cell-intrinsic and -extrinsic effects on B cell development, we next generated mixed BM chimeras. 30:70 mixes of CD45.1$^+$ WT and CD45.2$^+$ ZIP7$^{P198A/P198A}$ or CD45.2$^+$ WT whole BM cells were injected intravenously into lethally irradiated CD45.1$^+$ WT recipient mice. Eight weeks after BM transfer, our analysis confirmed a B cell intrinsic block in development, which was most evident in a failure to progress from the late pre-B (FrD) to immature B (FrE) cell stage, with no residual mutant cells in the recirculating FrF population (Fig. 4d). This developmental block was mirrored in the spleen with progressive loss of transitional B cells from T1 to T3 (Fig. 4d); whereas ZIP7-mutated CD4+ and CD8+ T cells in thymus and spleen were not disadvantaged relative to WT cells (Supplementary Fig. 3). We cannot exclude a cell-intrinsic effect during the early pre-B cell stage (FrC), which might have been masked due to the small numbers of cells and difficulty of gating on CD45 allotypes at this stage. Mutant and WT immature B cells expressed kappa and lambda chains in similar ratios (90% kappa and 5% lambda in mutant compared to 95% and 5% in WT), excluding a defect in the light chain rearrangement machinery.

To gain a better understanding of the impact of ZIP7 hypofunction on B cell development, we flow-sorted 100-cell aliquots of each of the Hardy fractions from ZIP7$^{P198A/P198A}$ and WT mice for RNA-seq, and were able to obtain good quality RNA from B220$^+$CD43$^+$CD24$^+$BP1$^-$ pro-B (FrB), late pre-B (FrD) and immature B cells (FrE) (Fig. 5a and Supplementary Figs. 4 and 5). Focusing on transcripts that are modulated during mouse B cell development in ImmGen (www.immGen.org), we observed a systematically altered pattern of gene transcription consistent with developmental delay in ZIP7-deficient pre-B and immature B cells, but not at the earlier pro-B stage. Thus, the few ZIP7-deficient cells bearing the surface markers of FrE had in fact failed to exit fully from the transcriptional profile of FrD and, likewise, ZIP7-deficient cells in FrD abundantly expressed transcripts normally associated with FrC (Fig. 5a and Supplementary Fig. 5). In contrast, few transcripts were differentially expressed between WT and ZIP7-deficient FrB and these did not follow a pattern of developmentally coordinated gene expression (Supplementary Fig.

4). The analysis showed no statistically significant difference in expression of other ZIP and ZnT transporters in Fr D and E (see materials and methods).

ZIP7-deficient immature B cells continued to express *Rag* and *Il7r* genes, and failed to upregulate characteristic FrE transcripts such as *Tnfrsf13c* (BAFFR) and *Ms4a1* (CD20) (Fig. 5a). This indicates a failure of the normal transition from late pre-B to immature B cells, at which stage constitutive BCR signalling would normally repress FOXO1-dependent genes involved in light chain gene rearrangement (*Rag1/2* and *Irf4*) and cell proliferation (*Il7r*), followed by upregulation of proteins including BAFFR that mediate peripheral survival signals[19, 20]. These key findings were confirmed at the protein level by flow cytometry, including the failure to downregulate IL7Rα (CD127; Fig. 5b) and upregulate BAFFR and CD20 (Fig. 5c). The same developmental blockade was observed in BM samples from both patients that were compound heterozygous for the P190A and E363K variants (Fig. 5d). Thus, in contrast to BTK deficiency, ZIP7 mutation subverts both mouse and human B cell development in a profound and conserved manner.

Reduced cytoplasmic Zn^{2+}

Given that ZIP7 allows the cytoplasmic ingress of Zn^{2+} from the ER, we reasoned that its impaired function would alter Zn^{2+} distribution in developing B cells, reducing its availability in the cytoplasm. To provide sufficient material to investigate this hypothesis, we generated B cell lines from WT and P198A homozygous mutant mouse BM maintained in IL-7- enriched media. WT and mutant cells cultured in these conditions showed comparable proliferation and differentiation to a predominantly $CD43^+CD24^+BP-1^{+/-}$ phenotype, which is considered equivalent to Fractions B-C-C' in B cell development[21, 22]. The withdrawal of IL-7 and addition of BAFF to these cultures increased the survival of IgM^+IgD^- immature and IgM^+IgD^+ mature B cells from WT but not from mutant cells (Fig 6a). In this way, the model system recapitulated the developmental block seen *in vivo*.

To measure the cytoplasmic and ER concentrations of Zn^{2+} at the point of blockade, we transduced aliquots of IL-7-cultured cells with either the cytoplasmic or the ER-targeted versions of Zn^{2+} FRET reporters, eCALWY-4 (K_d 630 pM) or eCALWY-6 (K_d 2.9 nM)[16, 23]. We then measured the relative cytoplasmic and ER concentrations of Zn^{2+} in propidium iodidenegative WT and mutant cells (>95%) using FRET-fluorescence lifetime imaging microscopy (FRET-FLIM)[24]. An advantage of this approach is that lifetime imaging is independent of the concentration of measured fluorophore, and hence free Zn^{2+} concentrations can be compared independently of reporter expression[24]. Cytoplasmic Zn^{2+} concentrations were indeed lower in mutant compared to WT cells, whereas ER Zn^{2+} amounts were equivalent (Fig. 6b and c).

In this system, the spatial distribution of cytoplasmic Zn^{2+} appeared uniform in the steady state in both WT and mutant B cells (Fig. 6b). However, local variations in Zn^{2+} concentration would most likely be beyond the temporal and spatial resolutions of the current FRET-FLIM approach. It was therefore of interest to investigate the spatial distribution of endogenous ZIP7 in the relevant cell type, taking advantage of a sensitive and specific anti-human-ZIP7 antibody. Using stimulated emission depletion (STED) microscopy, we observed that >50% ZIP7-containing structures lay within 1μm (and 25%

within 250nm) of the plasma membrane of activated human primary B cells, in contrast to the wider distribution seen in the cytoplasm of the much larger HEK293T cells (Fig. 6d - f). Thus local and/or dynamic changes in Zn^{2+} distribution related to ZIP7 might differ between cell types.

Developmental arrest is linked to a survival defect

In principle, the failure of ZIP-mutated B cells to complete their development could reflect a lack of requisite survival signals via the (pre-)BCR and/or accessory pathways, or excessive toxicity. Although we had failed to observe an excess of free Zn^{2+} in the ER of B cells from the ZIP7[p198A/p198A] mice, we considered the possibility that zinc loading of the ER could nonetheless drive an unfolded protein response (UPR), as recently described in the gut and skin of gene-targeted mice with tissue-specific ZIP7 knockout[25, 26]. However, our RNA-seq data revealed no evidence of an UPR transcriptional signature in the mutant pre-B or immature B cells, nor was *Xbp1* splicing altered (Supplementary Fig. 6a). Therefore, while the UPR may underlie some of the extra-hematopoietic effects of ZIP7 deficiency, it is not limiting in B cells.

We next asked whether expression of the anti-apoptotic survival factor B-cell lymphoma 2 (BCL2) could rescue B cell development at the pre-B to immature stage in ZIP7[P198A/P198A] mice. Introduction of a B cell specific *Bcl2* transgene (from C57BL/6-Tg(BCL2)22Wehi/J)[27] increased peripheral B cell numbers in both WT and ZIP7[P198A/P198A] mice but did not relieve the developmental block (Supplementary Fig. 6b-e). This suggested that ZIP7 deficiency was not simply accelerating the death of otherwise normally developing B cells, but was fundamentally impairing the process of B cell differentiation, in keeping with the systematically altered program of gene expression detected by RNAseq.

Intact ZIP7 is required for BCR signalling

Given that Ig heavy chain expression is required for the transition from pro-B to pre-B[28] and Ig light chain expression for the pre-B to immature B cell transition[29], we considered the possibility that ZIP7 deficiency impaired (pre-)BCR expression or signalling. To bypass the need for DNA recombination by RAG1/2 at both pro-B and pre-B cell stages, we crossed ZIP7[P198A/P198A] mice with animals expressing a transgenic anti-hen egg lysozyme (anti-HEL)-specific BCR (SW[HEL] mice)[30]. This generated WT and ZIP7[P198A/P198A] immature SW[HEL] B cells expressing equivalent levels of surface BCR (Fig. 7a-c), enabling us to interrogate the integrity of the downstream signalling pathway. Despite normal BCR expression (Fig. 7c), ZIP7[P198A/P198A] B cells still failed to mature normally, as indicated by lower cell numbers in the spleen (Fig. 7b) and an inability to upregulate CD20 and BAFFR (Fig. 7c). Moreover, when exposed to soluble HEL (sHEL) antigen or to anti-IgM, immature ZIP7[P198A/P198A] SW[Hel] B cells showed impaired antigen-induced signalling as judged by reduced amounts of multiple phosphorylated intermediates, including SYK, PLCγ2 and ERK (Fig. 7d and e). This effect was specific to B cells because signalling was unaffected in developing T cells (Supplementary Fig 7).

A priori, these complex effects on pathways downstream of the BCR could be mediated by variation in kinase or phosphatase activity. Since Zn^{2+} is widely reported to be a negative

regulator of phosphatases[31,32], the diminished cytoplasmic Zn^{2+} associated with ZIP7 deficiency could be expected to cause pathologically elevated phosphatase activity, and thus contribute to impaired pre-BCR- and BCR-dependent signalling at the positive selection check-points. Constitutive phosphatase activity was indeed higher in ZIP7[P198A/P198A] compared to WT pre-B and immature B cells, as measured by flow cytometry using a cell-permeable alkaline phosphatase substrate (Fig. 8a and b). The phosphatase and tensin homolog (PTEN) is among the phosphatases previously described as being inhibited by Zn^{2+}, lies upstream of FOXO1-dependent signalling[33], and contributes to the basal phosphatase activity measured in developing B cells (Supplementary Fig. 8a). Progressive inhibition of PTEN with its specific inhibitor BpV(phen) also revealed lower amounts of constitutive signalling to SYK, PLCγ2 and ERK in immature ZIP7[P198A/P198A] SW_{HEL} B cells compared to WT SW_{HEL} B cells (Fig. 8c), but not in developing T cells (Supplementary Fig 7d-f), in keeping with constitutively increased phosphatase and/or lower basal kinase activity during the stage of B cell positive selection. We could detect no variation in kinase gene expression (equivalent transcription of SYK, BLNK, PLCγ2 and ERK in FrE by RNA-seq); and no difference in protein expression of PLCγ2, which we were able to detect reliably by flow cytometry (Supplementary Fig. 8b). However, crossing ZIP7[P198A/P198A] mice to mice with B cell specific haploinsufficiency of PTEN could not reverse the block in B cell development (Supplementary Fig. 8c and d). These data indicate that the regulation of positive selection by ZIP7 is due to effects on multiple pathways.

Discussion

Our studies identify a novel form of autosomal recessive agammaglobulinemia caused by hypomorphic mutations in the ER-to-cytoplasmic zinc transporter ZIP7. This discovery implicates Zn^{2+} as the third divalent cation associated with a human immunodeficiency. Despite zinc's status as a key player in protein structure and function, we are at an early stage in understanding its broader roles in homeostasis and human disease. Its tight control by buffering, and the diversity of Zn^{2+} transporters, indicate that dynamic regulation of Zn^{2+} distribution is critical. This conclusion is supported by knowledge that mutations in the human plasma membrane Zn^{2+} transporter, *SLC39A4* (ZIP4), cause total body Zn deficiency and a separate but related disease, acrodermatitis enteropathica[34]. As well as a pathognomonic dermatitis and a variable enteropathy, it is noteworthy that Zn deficiency causes lymphopenia, with accelerated apoptosis of developing B cells[35].

Importantly, the *SLC39A7* (ZIP7) disease alleles are hypomorphic and exhibit partial loss of ZIP7 function. It was recently reported that complete loss of ZIP7 in cell lines causes a reduction in cytoplasmic Zn^{2+} and an increase in ER Zn^{2+} concentrations as quantified by mass spectrometry[36]; and our findings show that germline null mutations are embryonic lethal in the mouse. Tissue-specific ZIP7 knock-out in the gut of mice by cre-mediated gene deletion reduces intestinal epithelial cell self-renewal and is associated with an ER stress phenotype[25]. ER stress is also caused by null mutations of catsup, the *Drosophila* ZIP7 homologue[37]; and loss of Ke4, which is the ZIP7 homologue in zebrafish, results in eye, brain and skeletal malformations[38]. We postulate that residual ZIP7 function in patients protects these tissues from the effects of extreme Zn^{2+} redistribution including ER stress.

Our findings emphasise the specific sensitivity of mammalian B cell development to perturbations of Zn^{2+} homeostasis. Whereas most tissues tolerate partial ZIP7 deficiency, developing B cells are profoundly affected and fail to progress beyond the pre-B-cell stage. Such developmental blockade is characteristic of over 90% of primary agammaglobulinemias, which are typically associated with specific impairment of pre-BCR and/or BCR signalling[4]. Our data suggest that ZIP7 hypofunction likewise impedes signalling by the nascent BCR during positive selection, and that this may be in part due to defective Zn^{2+}-dependent inhibition of phosphatase activity. In the chicken B cell line DT40, which does not possess a homologue of ZIP7, ZIP9-dependent Zn^{2+} transport was similarly reported to enhance BCR signalling by negatively regulating phosphatase activity[39]. CD74-cre mediated deletion of ZIP10, which transports Zn^{2+} across the plasma membrane, also reduced mature B cell numbers and BCR-induced B cell proliferation in mice; yet, paradoxically, this was reportedly associated with increased BCR signalling and reduced CD45 activity[11]. Unravelling these complex effects of individual transporters will require the development of improved reporters to resolve changes in Zn^{2+} levels dynamically and at higher spatial resolution.

The selective sensitivity of developing B cells to deficiency of one among several ubiquitously expressed Zn^{2+} transporters might be considered surprising, particularly given the substantial overlap of antigen receptor signalling pathways with T cells. Non-redundant features that distinguish BCR from TCR signalling might also sensitize developing B cells to altered Zn^{2+} distribution. One such distinction is the B cell-specific requirement for FOXO1 degradation in order to suppress RAG expression at each positive selection checkpoint [19, 40, 41]. Progression through these developmental stages requires the sequential integration of multiple signals, determined by the activity of kinases and phosphatases. Our data show how these effects are influenced by the intracellular transport of Zn^{2+} and how, in principle, Zn^{2+} may modulate other outcomes in a variety of signalling contexts.

Methods

Study subjects and clinical immunophenotyping

Children with humoral immunodeficiency and absent B cells and their relatives were recruited under research protocols approved by local ethical review (Newcastle and North Tyneside 1 Research Ethics Committee; Institutional Review Board of St. Jude Children's Research Hospital). Peripheral blood was evaluated in accredited clinical laboratories by standard methods, including flow cytometric immunophenotyping. Primary dermal fibroblast cultures were established from punch skin biopsies, as part of the routine diagnostic workup of P1 and P2, who also underwent bone marrow examination. Further clinical and laboratory details are provided as supplementary information (Supplementary Data table 1).

Animal Experiments

The generation and phenotyping of the ZIP7 mutant mice models was carried out in accordance with Animal [Scientific Procedures] Act 1986, with procedures reviewed by the clinical medicine animal care and ethical review body (AWERB), and conducted under

project licenses PPL30/2966 and PPL P79A4C5BA. Animals were housed in specific pathogen free conditions, with the only reported positives on health screening over the entire time course of these studies being for Helicobacter hepaticus and Entamoeba spp. All animals were housed in social groups, provided with food and water ad-libitum and maintained on a 12h light:12h dark cycle (150–200 lux cool white LED light, measured at the cage floor). Phenotyping experiments were not blinded or randomized and no animals were excluded from the study.

Mice

A CRISPR/Cas9 nuclease was designed against exon 2 of *Slc39a7* (5'-GTTACTTACCCAAGGCATGC-3') using the MIT CRISPR design tool (crispr.mit.edu), which encompassed the murine equivalent (Proline-198) of the human Proline-190 residue. The target site protospacer was cloned as a linker, which was formed by annealing two oligonucleotides (5'-CACCGTTACTTACCCAAGGCATGC-3', 5'-AAACGCATGCCTTGGGTAAGTAAC-3') into a sgRNA scaffold within the pX330-U6-Chimeric_BB-CBh-hSpCas9 plasmid (Addgene #42230) via the BbsI restriction site, generating plasmid pX330-ZIP7. A single stranded oligonucleotide (ssODN) (5'-CACCGCTCTCTGCTCCAGATCCTGCTCAGTTTTGCTTCCGGGGGGGCTCCTGGGTGATGCGTTCCTCCACCTCATCGCGCATGCATTGGGTAAGTAACTTGTGGGCTCCGCCTCAAAGGCTTAAGCGGTTTTGTTC-3') harboring the murine equivalent of the desired P190A (chr6_33169678_C_G) point mutation, together with a silent mutation used to mark the mutated allele with an *NsiI* restriction site, was used as a template for homology-directed repair. The activity of the CRISPR/Cas9 nuclease and the fidelity of the homology-directed repair were verified in mouse embryonic stem cells (JM8F6) electroporated with pX330-ZIP7 and ssODN.

For the generation of the P198A knock-in mouse model, C57BL/6J (B6) zygotes were microinjected with 20 ng/μl of sgRNA, 10 ng/μl NLS-Cas9 mRNA and 20 ng of ssODN. sgRNA was synthesized by *in vitro* transcription using the MEGAshortscript™ T7 Transcription Kit (ThermoFisher Scientific) from a DNA template to add a 5' T7 polymerase binding site, prepared by PCR amplification of the pX330-ZIP7 plasmid. Capped mRNA for NLS-Cas9 was generated by cloning the NLS-Cas9 cDNA from pX330-ZIP7 into pcDNA3.1, linearizing the plasmid with *XhoI* and using this as a template for *in vitro* transcription using the mMESSAGE mMACHINE® T7 Ultra Kit (ThermoFisher Scientific). *In vitro* transcribed RNAs were purified using the MEGAclear Kit (ThermoFisher Scientific) and diluted prior to microinjection in 10 mM Tris.HCl pH7.5, 0.1 mM EDTA pH 8.0. Microinjected zygotes were cultured overnight to the two-cell stage and surgically implanted into pseudopregnant CD1 females. Founder mice harboring the P198A allele in combination with putative loss-of-function alleles, were identified by genotyping using a PCR (5'-GTTCTTAATCGGTGGGAAGCTCC-3' and 5'-CAGCACACCAGTCCCTGGTTTT-3') amplifying a region of *Slc39a7* exon 2, followed by NsiI digestion to detect the incorporation of the template sequence. All founder mice were bred with WT C57BL6/J mice and the correct P198A allele, along with a number of putative loss-of-function indel alleles, were segregated in the resulting F1 offspring. Mice carrying the P198A, H199QV and *null* alleles were crossed to pure B6 for at least 6 generations (to

minimize the risk of co-segregating mutations caused by off target mutagenesis) and intercrossed to generate homozygotes and compound heterozygotes of the viable alleles.

BCL2 (C57BL/6-Tg(BCL2)22Wehi/J), swHEL *(C57BL/6-Igh^{Vh10-Brink}/J)*, Mb1Cre (Cd79b<tm1(cre)Reth), mice were maintained on the B6 background, PTEN floxed (PTEN^f) originated from the 129S1/SVimJ strain, were backcrossed to B6 for at least three generations. For BM chimeras, CD45.1$^+$ B6 mice were irradiated with two doses of 4.5 Gy spaced by 3 hours and injected with at least 5×10^6 BM cells of the indicated genotype (single samples or 30:70 mixture of WT B6.SJL CD45.1$^+$ BM and either ZIP7^{P198A} or WT B6 (CD45.2$^+$) BM). Mice were reconstituted for 8–10 weeks before immunization or analysis. All experiments included age and sex-matched littermate control animals. All experiments were approved by the NIHR or the Oxford University Ethical Review Committee and performed under UK Home Office Licence.

Zinc Supplementation

ZIP7 WT and P198A homozygous BM chimeras were given water with or without 0.5mM $ZnSO_4.7H_2O$ in drinking water for the full period of reconstitution of 8 weeks[42].

In vitro IgM stimulation

Cell suspensions from mouse BM were washed and suspended in 2% FCS RPMI. Cells were warmed at 37°C for 5min and incubated at 37°C (10^6 cells/well in 96w U bottom plates) with the indicated doses of anti-IgM F(ab)$_2$ (Jackson Immunoresearch), sHEL (Sigma) for 5 minutes, BpV(phen) (Sigma) for 30 minutes. Subsequent surface and intracellular staining were performed using the BD Cytofix/Cytoperm protocol.

Flow Cytometry

Cell suspensions from mouse BM (one femur and tibia), spleen, thymus, mesenteric lymph nodes and peritoneal cavity were counted on a hemocytometer and stained in FACS buffer (DPBS supplemented with 2%FCS, 0.05% Na Azide, HEPES 10 mM) for 30 minutes on ice.

HEL-binding cells were detected by incubating cells with 200 ng/ml of unlabelled HEL for 15 minutes on ice and counterstaining with HyHEL9 (a gift from Jason Cyster) conjugated to Pacific Blue. Intracellular staining was performed using the Cytofix/Cytoperm buffer (BD Bioscience) and the antibodies against phosphorylated epitopes. Data were acquired on a FACSCanto10c (BD) and analyzed with FlowJo Software (Tree Star).

mAbs against the following mouse antigens (clone) were purchased from Biolegend unless otherwise specified: B220 (RA3-6B2) AlexaFluor700, BV605, PE-Cy7, PerCP-Cy5.5; mouse BAFFR (7H22-E16) PE from BD; BP-1 PE from BD; CD3 (17-A2) BV421; CD4 (GK1.5) AlexaFluor700; CD8 (53-6.7) Per-CP-Cy5.5; CD8 (53-6.7) PerCP-Cy5.5 and PE; CD11b (M1/70) APC; CD11c (N418) FITC; CD19 (6D5) AlexaFluor700; CD20 (SA275A11) APC; CD21/35 (7E9) APC-Cy7; CD21/35 (7E9) BV605 from BD; CD23 (EBVCS-5) PE from BD; CD23 (B3B4) PE-Cy7; CD24 (M1/69) FITC, AlexaFluor700, BV605; CD25 (PC61) PE and BV421; CD43 (S7) APC and PerCP-Cy5.5 from BD; CD44

(IM7) FITC; CD45.1 (A20) PE-Cy7 and APC-Cy7; CD45.2 (104) APC, BV421 and BV605; CD62L (MEL14) APC; CD127 (A7R34) PE-Cy7 and APC; F4/80 (BM8) PE-Cy7; Ly6c (HK1.4) PerCP-Cy5.5; Ly6g (1A8) AlexaFluor700; NK1.1 (PK136) PE-Cy7; IgM (II/41) FITC from BD; IgM (RMM-1) BV421; IgD (11-26c.2a) APC-Cy7; pAKT-S473 (M89-61) APC from BD; pAKT-T308 (J1-223.371) PE from BD; pBLNK (J117-1278) FITC from BD; pERK (4B11B69) FITC; pPLCγ2 (K86-1161) APC from BD; pSYK (5F5) PE; and PLCγ2 (K86–1161) AF647 from BD.

mAbs against the following human antigens (clone) were purchased from BD Bioscience unless otherwise specified: CD10 (J5) FITC from Beckman Coulter; CD34 (8G12) FITC; sIgD (polyclonal) FITC from SBA; CD36 (CLB-IVC7) FITC from Sanquin; CD3 (SK7) FITC and PERCP-Cy5.5; CD19 (HIB19) FITC; CD19 (4G7) PE; cyIgM (polyclonal) SBA/ Agilent technologies; TdT (HT6) FITC from Agilent; CD20 (L27) PE; sIgM (polyclonal) PE from ITK/SBA; CD16 (B73.1) PE; CD56 (C5.9) PE from Zebra/Dako; CD13 (My7) PE from Beckman Coulter; CD33 (P67.6) PE; CD138 (B-A38) PE from Diaclone); cyCD79a (HM47) PE from Beckman Coulter; CyCD179a (VpreB) (4G7) PE from Beckman Coulter; CD33 (P67.6) PerCP-Cy5.5; CD16 3G8) PerCP-Cy5.5; CD19 (SJ5C1) PerCP-Cy5.5 and APC; CD22 (S-HCL-1) APC; CD71 (LO1.1) APC; CD38 (HB7) APC; and BAFF-R (11C1) APC-Cy7 from Biolegend.

Alkaline phosphatase activity was measured using the cell permeant Alkaline Phosphatase Live Stain (Thermo Fisher): briefly cells were washed twice in serum free DMEM with MEM Vitamins (Gibco) and Na pyruvate (Sigma), incubated at 37°C for 30' with the live stain diluted 1:500 in the same media; after two washes, cells were stained on ice for 15 minutes in FACS buffer and samples were immediately analyzed by flow cytometry.

Serum Immunoglobulin levels

Total murine serum IgG, IgM, IgA were measured using an ELISA quantitation kit from Bethyl Laboratories and following manufacturer instructions.

Whole exome sequencing

Genomic DNA from P1, P3, P4, P5 and P6 and the parents of P3, P4 and P6 was subjected to whole exome sequencing. Exome capture was performed with SureSelect Human All Exon kits (Agilent Technologies). Paired-end sequencing was carried out on a HiSeq 2500 sequencing system (Illumina) generating 100-base reads. Sequences were aligned to the GRCh37 reference build of the human genome, using the BWA aligner[43]. Downstream processing and variant calling were performed with the GenomeAnalysis Toolkit[44], SAMtools[45], and Picard. Substitution and InDel calls were made with the GATK Unified Genotyper. All variants were annotated with an annotation software system that was developed in-house[14]. Putative disease alleles were validated genetically by Sanger sequencing of patient and family genomic DNA.

RNA sequencing

Cell suspensions from freshly isolated BM were obtained from straight chimeras, 5 WT and 5 P198A/P198A mutants, 8 weeks after reconstitution, and sorted using a FacsARIA III

(BD), using the following gating strategy: viable, B220$^+$CD43$^+$CD45.1$^-$CD45.2$^+$CD24$^+$BP1$^-$ (FrB/pro-B); B220$^+$CD43$^-$CD45.1$^-$CD45.2+IgM$^-$IgD$^-$ (FrD/late preB) and viable, B220$^+$CD43$^-$CD45.1$^-$ CD45.2$^+$IgM$^+$IgD$^-$ (FrE/Immature). 100 cells per sample were directly sorted into ice cold cell lysis buffer (0.4% (vol/vol) Triton X-100 and 2 U/µl RNase inhibitor, 4×10^7 dilution of ERCC spike in control, comprising a pre-formulated blend of 92 transcripts, derived and traceable from NIST-certified DNA plasmids), 2.5 mM dNTPs (Thermo-Fisher), 2.5 µM Oligo (Oligo-dT30VN.) and immediately frozen in dry ice.

Sorted cells were processed using the Smart-seq2 protocol with minor changes[46]. Briefly, cDNA was quantified using the Agilent 2100 Bioanalyzer and tagmentation was performed using 1 ng of pre-amplified cDNA and 17 cycles of enrichment PCR. Indexing of the samples was performed using the Nextera XT DNA Sample Preparation Index kit (24 index primers, manufacturer (Illumina)), according to manufacturer's instructions. Following library preparation, the samples were sequenced on an Illumina HiSeq 4000 instrument as 75 bp paired-end reads. Bioinformatic analysis was performed using in-house pipelines and tools (https://github.com/CGATOxford/CGATPipelines) and [47]. Briefly, reads were aligned to the mm10 mouse genome using hisat2 version 2.1.0[48], and reads were quantified over feature annotations (ensemble81) using featureCounts program version 1.4.6 within the Subread software package[49]. DESeq2 was used for statistical analysis of the differential expression for each gene between WT and ZIP7$^{P198A/P198A}$ mice. A gene was considered differentially expressed if the log2 fold change was +/− 1 and significance value was P$_{adj}$ < 0.05, which was adjusted for FDR due to multiple testing procedures to control for type I error. Clustering and heat maps were generated in R with pheatmap package version 1.0.8. For heat maps, expression values were scaled per gene.

Cloning, expression and visualization of human *SLC39A7* alleles

SLC39A7 cDNA was amplified from total RNA extracted from EBV-transformed B cells and cloned in pCMV6-AC-myc-DDK plasmid between *AscI* and *NotI* (Origene). Mutagenesis was performed using the Quick Change Mutagenesis kit (Agilent Technologies). Expression of WT and mutant isoforms was assessed by immunoblotting total protein extracted (RIPA) 48 hours post-transfection (FuGENE$^®$ HD Transfection Reagent, Promega) with 500ng of plasmid into mycoplasma-free HEK293T cells. Anti-ZIP7 (HPA053999, Sigma Aldrich) and anti-Flag (F1804, Sigma Aldrich) antibodies were used for ZIP7 detection. Anti-GAPDH (5174, Cell Signaling) was used for normalization. Alternatively, ZIP7 was transfected into HEK293T cells on 8-well chamber slide (Merck Millipore PEZGS0816) pre-coated with Cell-tak (Fisher Scientific 10317081). Cells were later fixed with 4% formaldehyde in PBS (28906, ThermoFisher Scientific), permeabilized with 0.1% Triton-X in PBS, stained with primary anti-ZIP7 (HPA053999, Sigma Aldrich)/ anti-Flag (F7425, Sigma Aldrich), anti-Calnexin (610524B, Dbiosciences) and secondary goat anti-rabbit IgG Alexa Fluor 594 (A-11037, ThermoFisher Scientific), goat anti-mouse IgG Atto 647N (50185, Sigma Aldrich) antibodies, and visualized by confocal microscopy (Leica TCS SP8).

Primary B cells were isolated from whole blood donated by healthy individuals using RosetteSep™ Human B Cell Enrichment Cocktail. Purity of B cells was assessed by flow cytometry, and found >80% CD19 staining, <1% CD3 staining, <4% CD14 staining. B cells were activated by 50ng/ml IL-4 (204-IL, R&D Systems), 0.5μg/ml CD40 ligand (6420-CL, R&D Systems) and 10 μg/ml IgM (16-5099-85, Invitrogen) for at least 48 hours before seeding onto 8-well chamber slides pre-coated with Cell-tak. Cells were fixed with 4% formaldehyde in PBS, permeabilized with 0.1% Triton-X in PBS, stained with primary anti-ZIP7, anti-Calnexin and secondary goat anti-rabbit IgG Alexa Fluor 594, and goat anti-mouse IgG Atto 647N or goat anti-mouse IgG Abberior STAR 635P antibodies. HEK293T cells were stained by the same methodology. Images were acquired on a Leica TCS SP8 STED 3X point scanning confocal microscope with white light super continuum lasers and 3 STED depletion lasers (592 nm, 660 nm and 775 nm) using STED WHITE HC PL APO CS2 100x/1.40 OIL lens. The DAPI and AF488 channels were acquired in confocal mode while the AF594 and ATTO647 channels were acquired in confocal and STED mode.

Deconvolution, colocalization analysis and object analysis were performed with Huygens 18.04 from SVI (www.svi.nl). Proximity measurements were performed using the Advanced Object Analysis feature in Huygens. ZIP7 fluorescence signals were segmented into individual objects and the distance of their center of mass to the inner side of the plasma membrane was measured. Violin plots were prepared in R.

Primary Mouse BM B cell culture, transduction and BAFF dependent differentiation

IL-7-dependent BM cell lines were cultured as described[50]. Single cell suspensions were isolated from the femur and tibia of 3-4 week old mice. After RBC lysis, cells were incubated in DMEM supplemented with 10% FCS at 37°C, 5% CO_2 for 30 min. Non-adherent cells were transferred to 6-well plates, at 750,000 cells/ml, in RPMI supplemented with 20% FCS (R20), L-Glutamine, 2-mercapto-ethanol, non-essential amino acids, Na Pyruvate, MEM vitamins, penicillin/streptomycin, and IL-7 10 ng/ml (Peprotech). 1×10^6 cells were transferred to each well of a 6 well plate in a final volume of 4 ml/well. Half the enriched RPMI volume was replaced every 3 days. To initiate further differentiation, actively proliferating cells were then transferred to R20 without IL-7 but containing BAFF (Peprotech) 50-100ng/ml for 3-4 days, in the presence or absence of BpV(phen).

Primary B cell transduction and Fluorescence Resonance Energy Transfer – Fluorescence Lifetime Imaging microscopy (FRET-FLIM) in live cells

On day 7 of culture, IL-7-dependent BM cells were transduced with Zn^{2+} FRET biosensors eCALWY-4 and/or eCALWY-6 engineered with Cerulean (donor) and Citrine (acceptor)[51] targeted either to the cytosol or the ER. ER-eCALWY-4 and ER-eCALWY-6 are targeted to the ER by an N-terminal preproinsulin sequence and C-terminal Lys-Asp-Glu-Leu (KDEL) sequence. For the purposes of these experiments, the eCALWY constructs were cloned into retroviral pMX-DEST-puro-derived vectors. Filtered retroviral supernatants, harvested 48 hr following co-transfection of BOSC23 cells with 7 μg pCL-Eco and 7 μg pMX-DEST-puro-derived plasmids, were used to infect the cell cultures in the presence of polybrene (2.5 μg/ml) and HEPES (20 mM) by spinoculation (850 x *g* for 90 min at 30°C). After a rest

period of 4 to 6 hours, viral supernatants were removed, and replaced with IL-7-supplemented culture medium. Cultures were maintained in IL-7 media for up to 8-10 days.

Multicolor images were acquired 2-4 days post-transfection using a Leica SP8-X-SMD confocal microscope (Leica Microsystems) with a 63×/1.3 numerical aperture water immersion objective. IL-7-dependent BM B cells were allowed to adhere to poly-L Lysine coated 8 well ibidi chamber slides in phenol red-free RPMI immediately before imaging. Cerulean and Citrine were excited at 440 and 514 nm, respectively, and the fluorescence emission was detected using two hybrid detectors in photon counting mode at 460-500 and 520-560 nm, respectively. A third channel for Propidium Iodide (PI) was also set to evaluate cell death so that only live cells would be chosen for analysis. PI was detected using a HeNe 560 nm laser and a 570 – 630 nm emission employing a third HyD detector and the same water immersion 63X objective. Only cells positive for Zn biosensor expression and negative for PI (typically >80%) were pre-selected for FLIM acquisition. FRET detection for eCALWY-4 and 6 was based on the time domain FLIM experiments which were performed using a Time-Correlated Single Photon Counting (TCSPC) approach operated by the FALCON module (Leica Microsystems, Mainheim) integrated on the Leica SP8-X-SMD confocal microscope (Leica Microsystems). A 440 nm picosecond pulsed diode laser PDL 800-B (PicoQuant) tuned at 40 MHz was used to excite the donor (Cerulean) and the emitted photons passing through the 460-500nm emission filter and were detected using the internal hybrid detector in photon counting mode. At least 1000 photon events per pixel were collected in all cases (where each pixel = 152 nm × 152 nm) and the lifetime analysis was carried out using the Leica FALCON FLIM integrated software. The acquired fluorescent decays were fitted pixel by pixel binning the images to 4 and using a background subtraction of around 10-20 photons. A bi-exponential model[52] fixing the Cerulean lifetime to 3.05 ns[53] was employed to recover the fraction of interacting donor f_D[52], which was then used to recover the relative concentration of Zn^{2+} $(1 - f_D)$.

Assay of ZIP7 activity in Xenopus oocytes

Xenopus oocyte expression: *Xenopus laevis* frogs were purchased from the African Xenopus Facility (South Africa). Care and all experimental procedures were carried out in accordance with UK Home Office guidelines. Oocytes were prepared and maintained as described elsewhere[54]. *SLC39A7* plasmids (see above) were further engineered by addition of a RFP tag at the C terminus of either WT or mutant ZIP7. *SLC39A7* RNA was transcribed *in vitro* using the MegaScript T7 kit (Thermo) and 1 μg of *Xba* I linearized plasmid DNA as a template. 10 ng/oocyte of RNA were injected and oocytes were incubated 3-5 days at 18°C in Barth's solution.

Zn transport assay: Oocytes were incubated in 20 μM Zinquin (Enzo Life Sciences) for 30 min followed by 5 washes with Barth's solution. Zinquin-loaded oocytes were then incubated for 5 min in 100 μM $ZnCl_2$ and visualised using an inverted Nikon TiE microscope (excitation wavelength 380nm, emission wavelength 510 nm). Images were captured at 40x using an Andor iXON DU885 EM-CCD camera and Nikon Elements software (v4.5). Settings were kept constant throughout each experiment. Multiple images were acquired in parallel focal planes starting at the extracellular matrix of the oocyte and

scanning through to the pigmented vesicles, which lie just beneath the plasma membrane. After deconvolution of the images the zinquin signal was visible as discontinuous punctate staining within the intervening, superficial cytoplasm. To quantitate this, representative fields of 50×50 μM were specified and 3 adjacent focal planes (1.2 μM interval) were analysed together in ImageJ. To subtract background staining, ImageJ was used to specify the shape (size of 0.2-2μM, roundness 0.5-1) and intensity of the "particles" to be analysed and a composite measure of signal strength was obtained as the product of their area and intensity. At least oocytes were analyzed per condition in each of 4 experiments.

For immunoblotting, 1-5 oocytes were homogenized in 10 μl of homogenisation buffer (1% Elugent (Calbiochem) in 100 mM NaCl 20 mM Tris/HCl, pH 7.6) per oocyte. Samples were centrifuged at 16000 g for 3 min at RT, the supernatant was mixed with an equal volume of SDS gel loading buffer, and visualised by immunoblotting as described[55].

ER stress assay

cDNA from cells sorted using the aforementioned gating strategy was used in an XBP-1 splicing RT-PCR assay[56]. PCR products were run on a 2.5% agarose gel. Negative and positive controls were untreated MEFs or MEFs treated with 2 μg/ml tunicamycin (Tm) for 4h, respectively.

Statistics

GraphPad Prism Software was used for statistical analyses, and unpaired, two tailed Student's t tests were used for statistical comparison between groups, unless otherwise specifically mentioned.

Data availability statement

RNA-sequencing data generated for this study (fig 5, supplementary figs 4, 5) have been deposited in the Gene Expression Omnibus (GEO) under accession code GSE108178. Other data that support the findings of this study (including raw data supporting figs 1 and supplementary fig 1) are available from the corresponding authors upon request.

Supplementary Material

Refer to Web version on PubMed Central for supplementary material.

Acknowledgements

References

1. Vetrie D, et al., The gene involved in X-linked agammaglobulinaemia is a member of the src family of protein-tyrosine kinases. Nature, 1993 361(6409): p. 226–33. [PubMed: 8380905]

2. Tsukada S, et al., Deficient expression of a B cell cytoplasmic tyrosine kinase in human X-linked agammaglobulinemia. Cell, 1993 72(2): p. 279–90. [PubMed: 8425221]

3. Aw A and Brown JR, Current Status of Bruton's Tyrosine Kinase Inhibitor Development and Use in B-Cell Malignancies. Drugs Aging, 2017 34(7): p. 509–527. [PubMed: 28536906]

4. Conley ME, Genetics of hypogammaglobulinemia: what do we really know? Curr Opin Immunol, 2009 21(5): p. 466–71. [PubMed: 19651503]

5. Durandy A, Kracker S, and Fischer A, Primary antibody deficiencies. Nat Rev Immunol, 2013 13(7): p. 519–33. [PubMed: 23765059]

6. Conley ME, et al., Agammaglobulinemia and absent B lineage cells in a patient lacking the p85alpha subunit of PI3K. J Exp Med, 2012 209(3): p. 463–70. [PubMed: 22351933]

7. Feske S, et al., A mutation in Orai1 causes immune deficiency by abrogating CRAC channel function. Nature, 2006 441(7090): p. 179–85. [PubMed: 16582901]

8. Li FY, et al., Second messenger role for Mg2+ revealed by human T-cell immunodeficiency. Nature, 2011 475(7357): p. 471–6. [PubMed: 21796205]

9. Kambe T, Hashimoto A, and Fujimoto S, Current understanding of ZIP and ZnT zinc transporters in human health and diseases. Cell Mol Life Sci, 2014 71(17): p. 3281–95. [PubMed: 24710731]

10. Lichten LA and Cousins RJ, Mammalian zinc transporters: nutritional and physiologic regulation. Annu Rev Nutr, 2009 29: p. 153–76. [PubMed: 19400752]

11. Hojyo S, et al., Zinc transporter SLC39A10/ZIP10 controls humoral immunity by modulating B-cell receptor signal strength. Proc Natl Acad Sci U S A, 2014 111(32): p. 11786–91. [PubMed: 25074919]

12. Taylor KM, et al., Structure-function analysis of HKE4, a member of the new LIV-1 subfamily of zinc transporters. Biochem J, 2004 377(Pt 1): p. 131–9. [PubMed: 14525538]

13. Lek M, et al., Analysis of protein-coding genetic variation in 60,706 humans. Nature, 2016 536(7616): p. 285–91. [PubMed: 27535533]

14. Kircher M, et al., A general framework for estimating the relative pathogenicity of human genetic variants. Nat Genet, 2014 46(3): p. 310–5. [PubMed: 24487276]

15. Zhang T, et al., Crystal structures of a ZIP zinc transporter reveal a binuclear metal center in the transport pathway. Sci Adv, 2017 3(8): p. e1700344. [PubMed: 28875161]

16. Vinkenborg JL, et al., Genetically encoded FRET sensors to monitor intracellular Zn2+ homeostasis. Nat Methods, 2009 6(10): p. 737–40. [PubMed: 19718032]

17. Cong L, et al., Multiplex genome engineering using CRISPR/Cas systems. Science, 2013 339(6121): p. 819–23. [PubMed: 23287718]

18. Hardy RR, et al., Resolution and characterization of pro-B and pre-pro-B cell stages in normal mouse bone marrow. J Exp Med, 1991 173(5): p. 1213–25. [PubMed: 1827140]

19. Dengler HS, et al., Distinct functions for the transcription factor Foxo1 at various stages of B cell differentiation. Nat Immunol, 2008 9(12): p. 1388–98. [PubMed: 18978794]

20. Tussiwand R, et al., BAFF-R expression correlates with positive selection of immature B cells. Eur J Immunol, 2012 42(1): p. 206–16. [PubMed: 22028296]

21. Holl TM, Haynes BF, and Kelsoe G, Stromal cell independent B cell development in vitro: generation and recovery of autoreactive clones. J Immunol Methods, 2010 354(1–2): p. 53–67. [PubMed: 20109461]

22. Corfe SA, Gray AP, and Paige CJ, Generation and characterization of stromal cell independent IL-7 dependent B cell lines. J Immunol Methods, 2007 325(1–2): p. 9–19. [PubMed: 17599344]

23. Chabosseau P, et al., Mitochondrial and ER-targeted eCALWYprobes reveal high levels of free Zn2+. ACS Chem Biol, 2014 9(9): p. 2111–20. [PubMed: 25011072]

24. Maares M, et al., Characterization of Caco-2 cells stably expressing the protein- based zinc probe eCalwy-5 as a model system for investigating intestinal zinc transport. Journal of Trace Elements in Medicine and Biology, 2018 49: p. 296–304. [PubMed: 29395783]

25. Ohashi W, et al., Zinc Transporter SLC39A7/ZIP7 Promotes Intestinal Epithelial Self-Renewal by Resolving ER Stress. PLoS Genet, 2016 12(10): p. e1006349. [PubMed: 27736879]

26. Bin BH, et al., Requirement of Zinc Transporter SLC39A7/ZIP7 for Dermal Development to Fine-Tune Endoplasmic Reticulum Function by Regulating Protein Disulfide Isomerase. J Invest Dermatol, 2017 137(8): p. 1682–1691. [PubMed: 28545780]

27. Strasser A, et al., Bcl-2 expression promotes B- but not T-lymphoid development in scid mice. Nature, 1994 368: p. 457. [PubMed: 8133891]

28. Reth M and Nielsen P, Signaling circuits in early B-cell development. Adv Immunol, 2013 122: p. 129–75.

29. Levine MH, et al., A B-cell receptor-specific selection step governs immature to mature B cell differentiation. Proc Natl Acad Sci U S A, 2000 97(6): p. 2743–8. [PubMed: 10688906]

30. Phan TG, et al., B cell receptor-independent stimuli trigger immunoglobulin (Ig) class switch recombination and production of IgG autoantibodies by anergic self-reactive B cells. J Exp Med, 2003 197(7): p. 845–60. [PubMed: 12668643]

31. Brautigan DL, Bornstein P, and Gallis B, Phosphotyrosyl-protein phosphatase. Specific inhibition by Zn. J Biol Chem, 1981 256(13): p. 6519–22. [PubMed: 6165721]

32. Haase H and Maret W, Intracellular zinc fluctuations modulate protein tyrosine phosphatase activity in insulin/insulin-like growth factor-1 signaling. Exp Cell Res, 2003 291(2): p. 289–98. [PubMed: 14644152]

33. Plum LM, et al., PTEN-inhibition by zinc ions augments interleukin-2-mediated Akt phosphorylation. Metallomics, 2014 6(7): p. 1277–87. [PubMed: 24759986]

34. Kury S, et al., Identification of SLC39A4, a gene involved in acrodermatitis enteropathica. Nat Genet, 2002 31(3): p. 239–40. [PubMed: 12068297]

35. Fraker PJ and King LE, Reprogramming of the immune system during zinc deficiency. Annu Rev Nutr, 2004 24: p. 277–98. [PubMed: 15189122]

36. Woodruff G, et al., The Zinc Transporter SLC39A7 (ZIP7) Is Essential for Regulation of Cytosolic Zinc Levels. Mol Pharmacol, 2018 94(3): p. 1092–1100. [PubMed: 29980658]

37. Groth C, et al., Protein trafficking abnormalities in Drosophila tissues with impaired activity of the ZIP7 zinc transporter Catsup. Development, 2013 140(14): p. 3018–27. [PubMed: 23785054]

38. Yan G, et al., Slc39a7/zip7 plays a critical role in development and zinc homeostasis in zebrafish. PLoS One, 2012 7(8): p. e42939. [PubMed: 22912764]

39. Taniguchi M, et al., Essential role of the zinc transporter ZIP9/SLC39A9 in regulating the activations of Akt and Erk in B-cell receptor signaling pathway in DT40 cells. PLoS One, 2013 8(3): p. e58022. [PubMed: 23505453]

40. Ubieta K, et al., Fra-2 regulates B cell development by enhancing IRF4 and Foxo1 transcription. J Exp Med, 2017 214(7): p. 2059–2071. [PubMed: 28566276]

41. Kerdiles YM, et al., Foxo1 links homing and survival of naive T cells by regulating L-selectin, CCR7 and interleukin 7 receptor. Nat Immunol, 2009 10(2): p. 176–84. [PubMed: 19136962]

References for Online Methods

42. Geiser J, et al., Clioquinol synergistically augments rescue by zinc supplementation in a mouse model of acrodermatitis enteropathica. PLoS One, 2013 8(8): p. e72543. [PubMed: 24015258]

43. Li H and Durbin R, Fast and accurate long-read alignment with Burrows-Wheeler transform. Bioinformatics, 2010 26(5): p. 589–95. [PubMed: 20080505]

44. McKenna A, et al., The Genome Analysis Toolkit: a MapReduce framework for analyzing next-generation DNA sequencing data. Genome Res, 2010 20(9): p. 1297–303. [PubMed: 20644199]

45. Li H, et al., The Sequence Alignment/Map format and SAMtools. Bioinformatics, 2009 25(16): p. 2078–9. [PubMed: 19505943]

46. Picelli S, et al., Full-length RNA-seq from single cells using Smart-seq2. Nat Protoc, 2014 9(1): p. 171–81. [PubMed: 24385147]

47. Sims D, et al., CGAT: computational genomics analysis toolkit. Bioinformatics, 2014 30(9): p. 1290–1. [PubMed: 24395753]

48. Kim D, Langmead B, and Salzberg SL, HISAT: a fast spliced aligner with low memory requirements. Nat Methods, 2015 12(4): p. 357–60. [PubMed: 25751142]

49. Liao Y, Smyth GK, and Shi W, featureCounts: an efficient general purpose program for assigning sequence reads to genomic features. Bioinformatics, 2014 30(7): p. 923–30. [PubMed: 24227677]

50. Holl TM, Haynes BF, and Kelsoe G, Stromal Cell-Independent B-Cell Development In Vitro: Generation and Recovery of Autoreactive Clones. Journal of immunological methods, 2010 354(0): p. 10.1016/j.jim.2010.01.007.

51. Hessels AM, Taylor KM, *and* Merkx M, Monitoring cytosolic and ER Zn(2+) in stimulated breast cancer cells using genetically encoded FRET sensors †*Electronic supplementary information (ESI) available. See DOI:* 10.1039/c5mt00257e *Click here for additional data file* Metallomics, 2016 8(2): p. 211–217. [PubMed: 26739447]

52. Padilla-Parra S, et al., Quantitative FRET analysis by fast acquisition time domain FLIM at high spatial resolution in living cells. Biophys J, 2008 95(6): p. 2976–88. [PubMed: 18539634]

53. Merola F, et al., Newly engineered cyan fluorescent proteins with enhanced performances for live cell FRET imaging. Biotechnol J, 2014 9(2): p. 180–91. [PubMed: 24357633]

54. Markovich D, Expression cloning of membrane proteins in _Xenopus_ oocytes. 2007 Protocol Exchange (2007) doi:10.1038/nprot.2007.331.

55. Turk E, et al., Membrane topology of the human Na+/glucose cotransporter SGLT1. J Biol Chem, 1996 271(4): p. 1925–34. [PubMed: 8567640]

56. Yoshida H, et al. XBP1 mRNA Is Induced by ATF6 and Spliced by IRE1 in Response to ER Stress to Produce a Highly Active Transcription Factor. Cell, 2001 107(7): p. 881–891. [PubMed: 11779464]
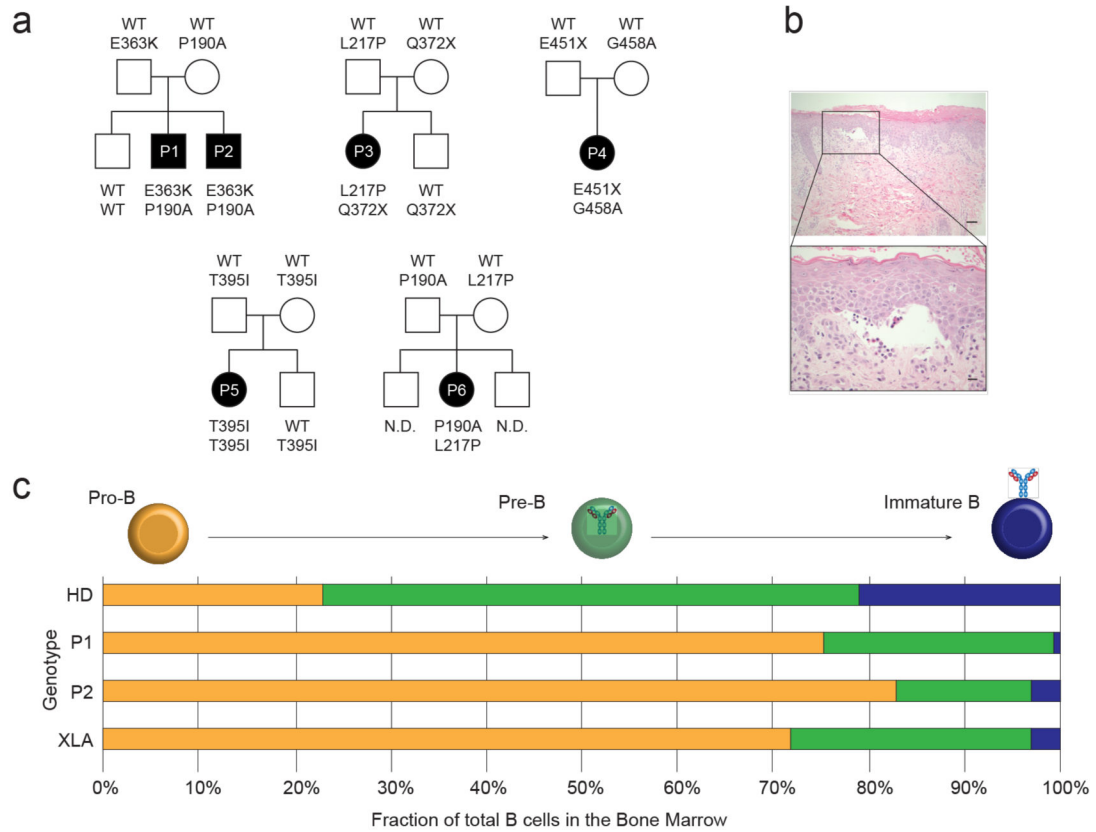
Figure 1. A novel autosomal recessive agammaglobulinemia caused by mutations in ZIP7.
(**a**) Pedigrees of five unrelated kindreds in which subjects with agammaglobulinemia and
absent B cells (P1-P6) carry the indicated *SLC39A7* (ZIP7) alleles. (**b**) Representative low
(scale bar 40 μm) and high-power (scale bar 10 μm) images of skin biopsy from patient P1
stained with hematoxylin and eosin, highlighting blister formation at the dermo-epidermal
junction (n=2). (**c**) Schematic representation of the B cell precursor compartments within the
BM of 9 age-matched healthy donors (HD), patients P1 and P2 (mutated ZIP7), and 12
disease controls with X-linked agammaglobulinemia (XLA), assessed by flow cytometry.
Pro-B cells are defined as CD22$^+$CyCD79a$^+$CyIgM$^-$; pre-B cells are CD22$^+$CyCD79a
$^+$CD10$^-$ CyIgM$^+$sIgM$^-$ and immature B cells are CD22$^+$CD19$^+$CyCD79a$^+$sIgM$^+$sIgD$^-$.
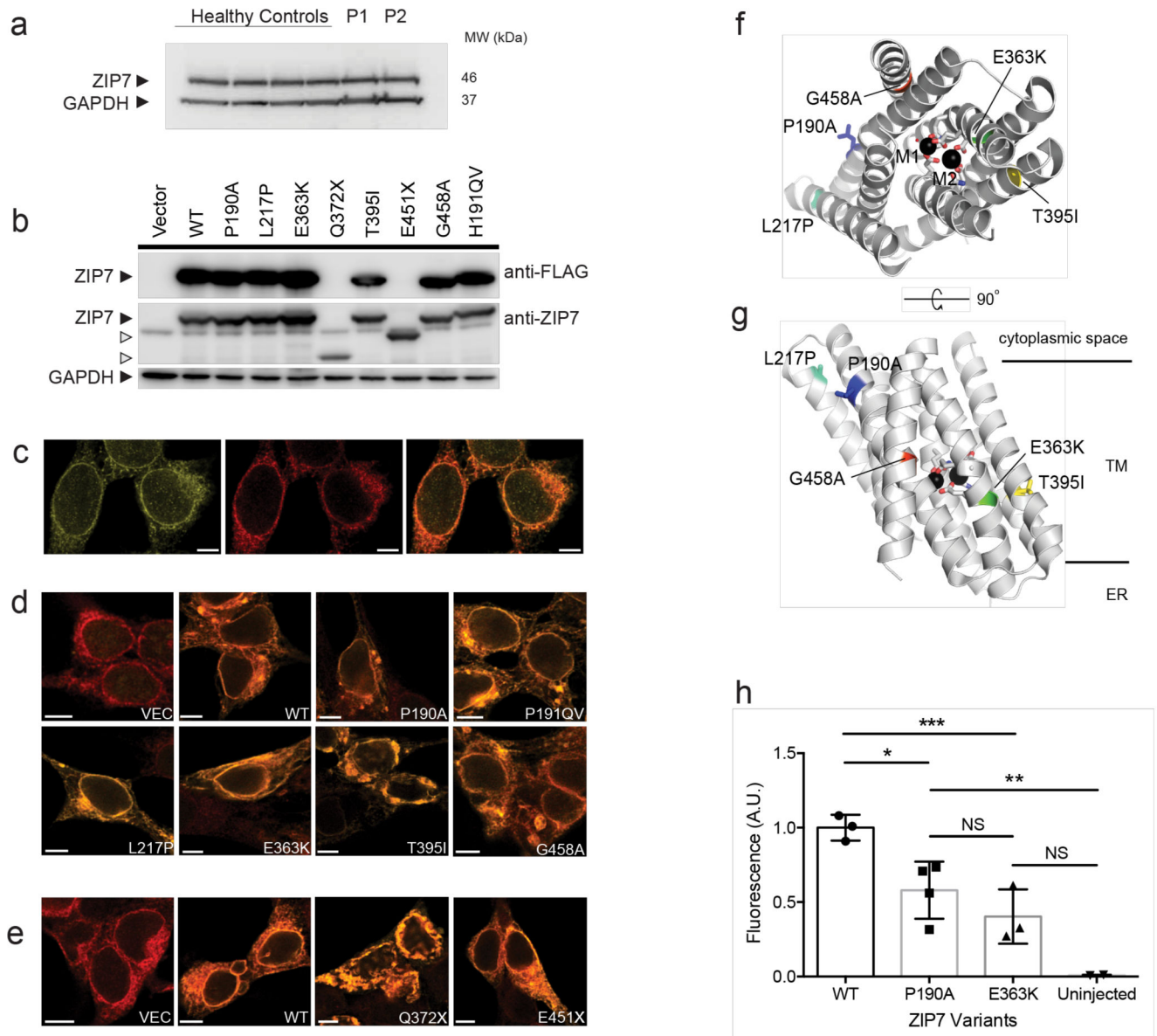
Figure 2. Multiple loss-of-function mutations in ZIP7.
(**a**) immunoblot (IB) of crude lysates from dermal fibroblasts of four healthy controls and two patients, P1 and P2, probed for ZIP7 protein and GAPDH. (**b**) IB of crude lysates from HEK-293T cells transfected individually with FLAG-tagged WT (WT) or mutant *SLC39A7* alleles, probed for ZIP7 or DDK epitopes, or GAPDH. H191ins corresponds to H199QV in mouse. Images in **a** and **b** are representative of 3 and 4 independent experiments, respectively. (**c**) Immunofluorescence images of HEK293T cells showing endogenous ZIP7 (left, green), ER marker calnexin (middle, red) and both ZIP7 and calnexin together (right, colocalization shows as orange signal). (**d**) The distribution of recombinant FLAG-tagged WT (WT) or indicated missense ZIP7 proteins in HEK293T cells, transfected individually and probed with primary antibodies against FLAG (green) and calnexin (red; orange signal thus indicates colocalization in the ER). Scale bar, 10μm. (**e**) As in **d**, but recombinant

truncation mutants were not FLAG-tagged so were probed with primary anti-ZIP7 antibody. Images (**c-e**) are representative of 3 independent experiments and Pearson coefficients were uniformly >0.6. (f and g) The location of missense mutations within the predicted protein structure of ZIP7, modelled on the structure of Bordetella pertussis ZIP using PyMOL; (**f**) *en face* and (**g**) side view of ZIP7. M1 and M2 represent Zn^{2+} ions bound within the channel, TM indicates transmembrane region. (**h**) Hypomorphic human *SLC39A7* alleles were expressed in *Xenopus* oocytes and ZIP7-mediated Zn^{2+} flux revealed following exposure of Zinquin-loaded oocytes to extracellular zinc (see Methods). Normalized mean fluorescence signal intensity is shown with SD for one experiment, (WT, n=3 oocytes; P190A, n=4; E363K, n=3, uninjected, n=2), representative of 4 independent experiments. Statistical comparison was by one-way ANOVA with Tukey's post-hoc test (DF=8); *p=0.0309; **p=0.0120; ***p=0.0066; NS, non-significant.
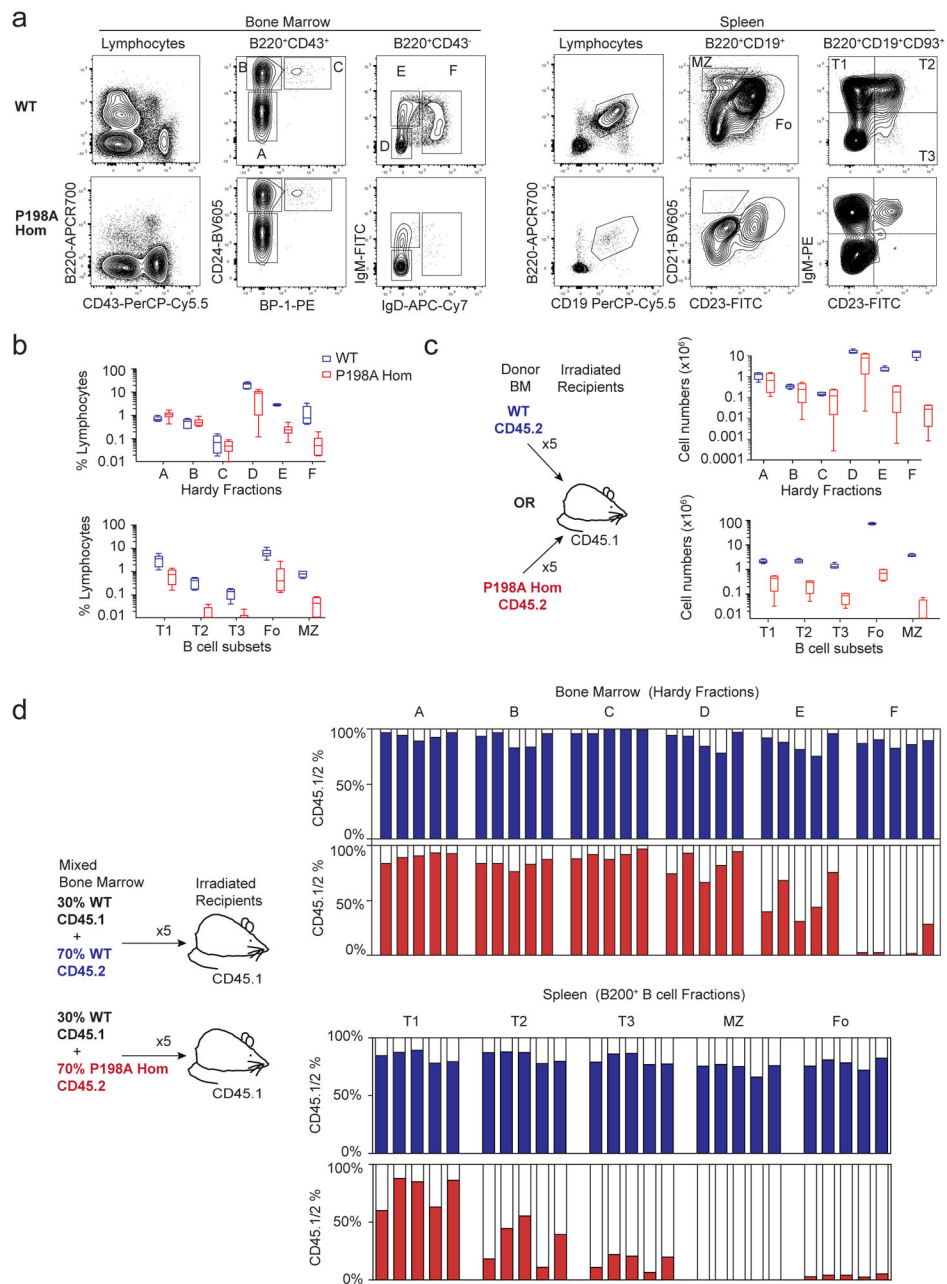
Figure 3. Generation of an allelic series of ZIP7 mutant mice.
(**a**) Site-directed mutagenesis of *SLC39A7* (ZIP7) in mouse zygotes using CRISPR/Cas9 to insert the P198A mutation and coincidentally generate an allelic series by homologous recombination (HR) and non-homologous end joining (NHEJ), here showing the WT, Zip7^{P198A} (P198A), Zip7^{H199QV} (H199QV) and Zip$^−$ (null) alleles. (**b**) Total B220$^+$ cell population as percentage of lymphocytes in the BM of 25-day-old mice, where circles represent individual mice (n=27 WT, 6 H199QV Hom; 13 P198A/H199QV and 18 P198A Hom); data are pooled from 6 independent experiments; bars are mean and 95% confidence intervals (CI) and comparison is by one-way ANOVA (F=51.71; DF=63) *= p<0.0001. (**c-d**) The appearance (**c**) and weight (**d**) of 3-4-week-old mice of different genotypes, where circles in (d) represent individual mice (n=74 WT, 14 H199QV Hom; 30 P198A/H199QV and 31 P198A Hom); weights were collected over time; bars are mean and 95% CI, and comparison is by one-way ANOVA (F=50.23; DF=148)*=p<0.0001. (**e**) Phenotypes associated with combinations of ZIP7 alleles.

Figure 4. ZIP7 deficiency leads to a B cell-intrinsic failure in development.
(**a**) Representative flow cytometry of B cell development in BM and spleen of WT and
P198A-Hom mice, gating on Hardy Fractions (Fr) A-F in the BM and total B220+CD19+ B
cells in the spleen. (**b**) B cell subsets as a percentage of lymphocytes in the BM (two femurs
and two tibias, upper panel) and in the spleen (lower panel), gating on
CD19+B220+CD93+IgM+CD23− T1, CD19+B220+CD93+gM+CD23+ T2 and
CD19+B220+CD93+IgM^{dim}CD23+ T3 transitional B cells, B220+CD19+CD23+CD21^{dim}
follicular B cells) and B220+CD19+CD23+CD21^{hi} marginal zone (MZ) B cells. n= 6 mice
per genotype, bars show means and 95% CI, representative of 5 independent experiments.
(**c**) Absolute numbers of B cell subsets in the BM (upper panel) and spleen (lower panel)

from lethally irradiated CD45.1 mice reconstituted for 8 weeks with CD45.2 WT or P198A-Hom BM (gated as in a). n= 5 mice per genotype, bars show means and 95% CI, are representative of 3 independent experiments. (**d**) The relative proportion of B cell subsets in BM (above) and spleens (below) of lethally irradiated mice reconstituted for 8 weeks with 70:30 mixtures of WT or P198A-Hom CD45.2[+] and WT CD45.1[+] BM (gated as in a). Each bar represents one mouse; filled columns show percentage CD45.2^{+} cells; data are representative of 3 experiments.
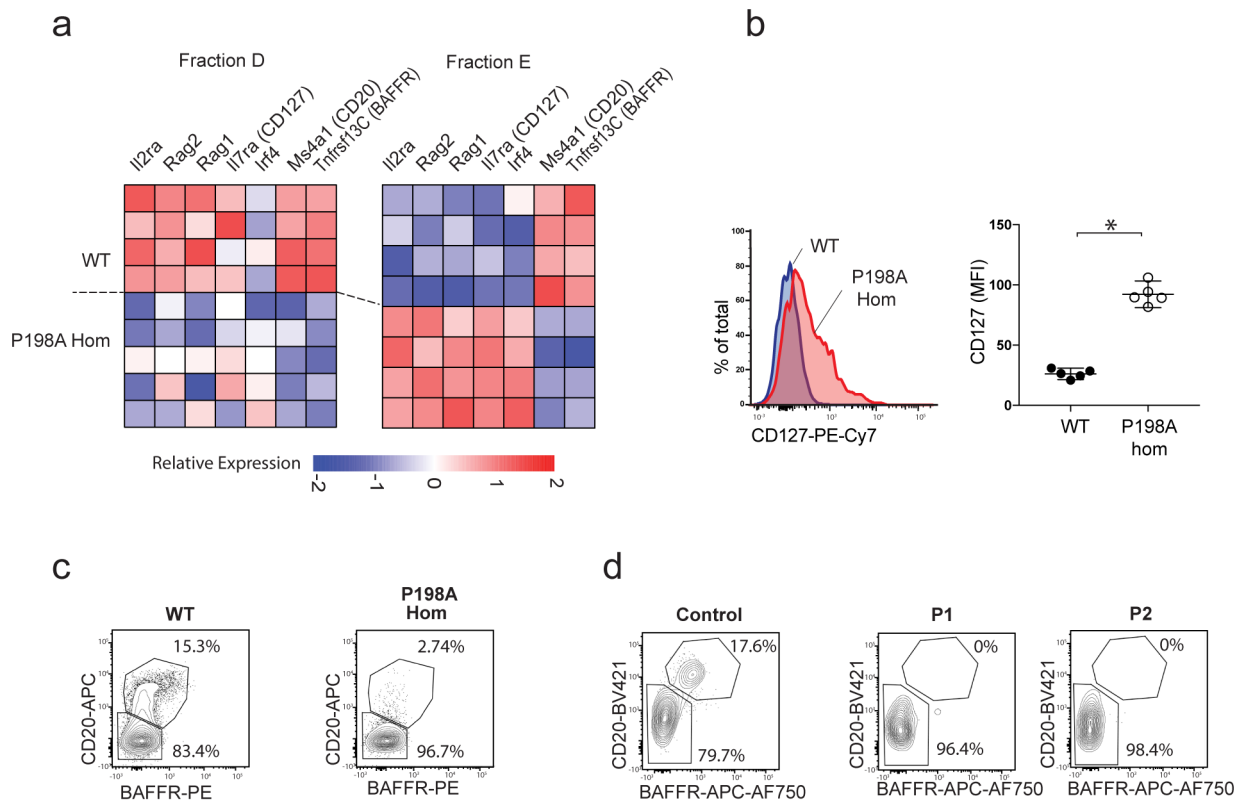
Figure 5. ZIP7 deficiency leads to developmental arrest at the late pre-B to immature B cell transition.

(**a**) Heatmap showing relative abundance of selected differentially expressed transcripts in sorted B cells from Fr D and E in WT and P198A-Hom mice, where rows represent individual mice. (**b**) Median CD127 expression on WT and P198A-Hom B cells from FrE, with representative histogram (left); graph (right) shows median expression in individual mice (n=5 per genotype), bars are means and 95% CI; comparison by unpaired t test, *=p<0.0001 (representative of 3 independent experiments). (**c-d**) BAFFR and CD20 staining in murine B cells from FrD (**c**) and human pre-B cells (**d**) comparing P198A-Hom and WT mice (representative of 3 independent experiments, with n=5 mice per genotype), affected humans (P1 and P2) and a control.
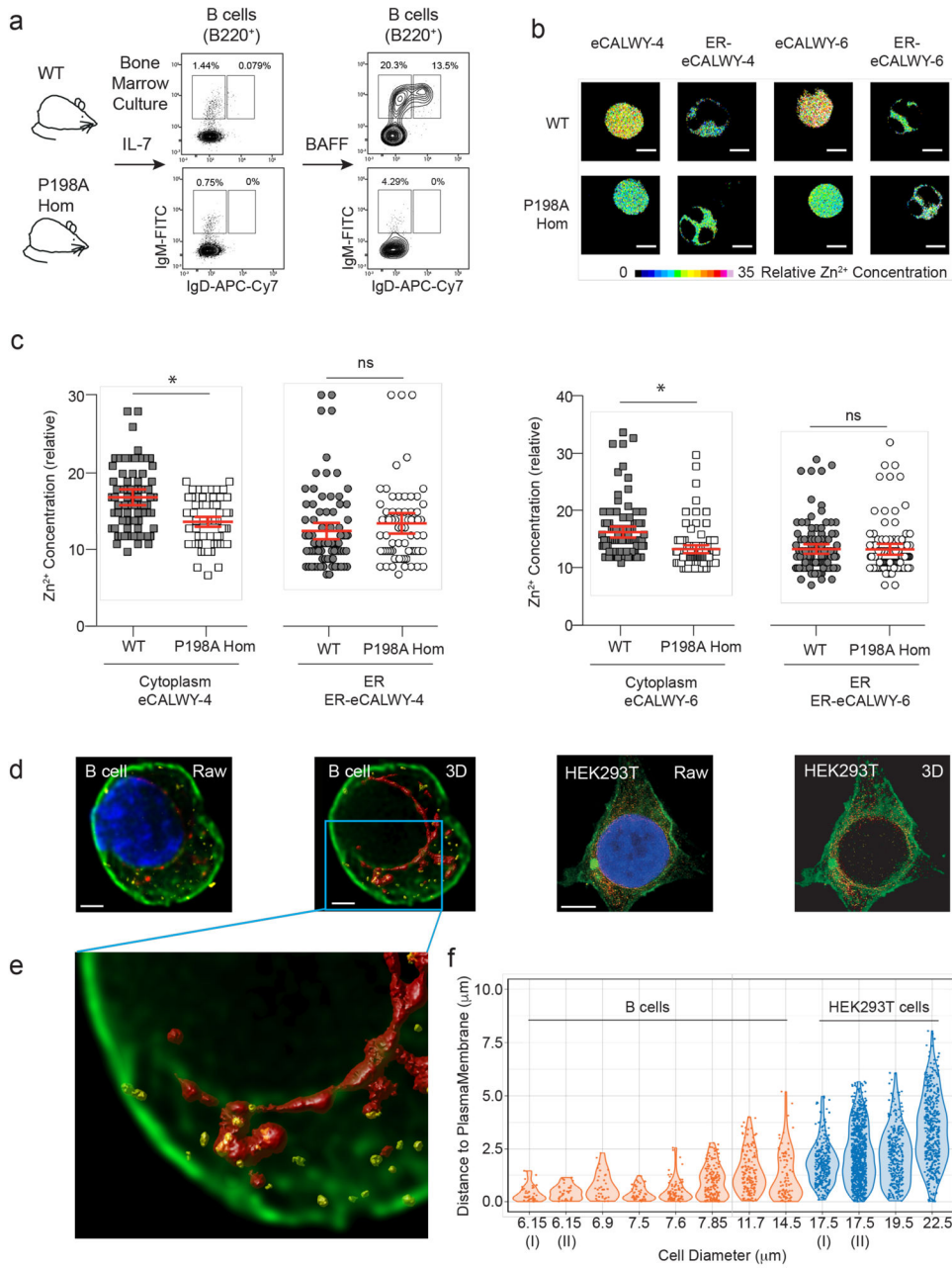
Figure 6. Reduced cytoplasmic zinc in the presence of ZIP7 mutation.
(**a**) WT and P198A-Hom IL-7 dependent B cell lines, showing representative flow cytometry before and after stimulation with BAFF. (**b**) FLIM fluorescent decays images of Zn^{2+} in IL-7-dependent WT and P198A-Hom B cells transduced with the cytoplasmic eCALWY-4 and eCALWY-6 and ER ER-eCALWY-4 and ER-eCALWY-6 Zn^{2+} reporters. Samples are representative of cells with the mean Zn^{2+} concentrations in (**c**), and scale bar 5 μm. Relative Zn^{2+} concentration proportional to a color scale showing theoretical reporter occupancy. (**c**) Relative Zn^{2+} concentration in cytoplasm and ER of IL-7 dependent WT and P198A-Hom cells expressing eCALWY-4 and eCALWY-6 reporters. Dots represent the FLIM fluorescent decay in individual B cells, with data pooled from three independent experiments

(*=p<0.0001); bars are means with 95% CI and comparison by t Test. **(d-e)** Super-resolution micrographs of activated primary human B cells or HEK293T cells, stained for endogenous ZIP7 (yellow), calnexin (red) and surface membrane (green). (**d**) Paired raw and deconvolved, 3D-rendered images are shown for B cells (left, scale bar 1 μm) and HEK293T cells (right, scale bar 5 μm). (**e**) Detailed view of indicated area in (**d**). (**f**) Violin plot depicting minimum distance from the centre of each ZIP7+ve "particle" to the plasma membrane of individual B (n=8) or HEK293T (n=4) cells, visualized as in (**d-e**); representative of 2 independent experiments.
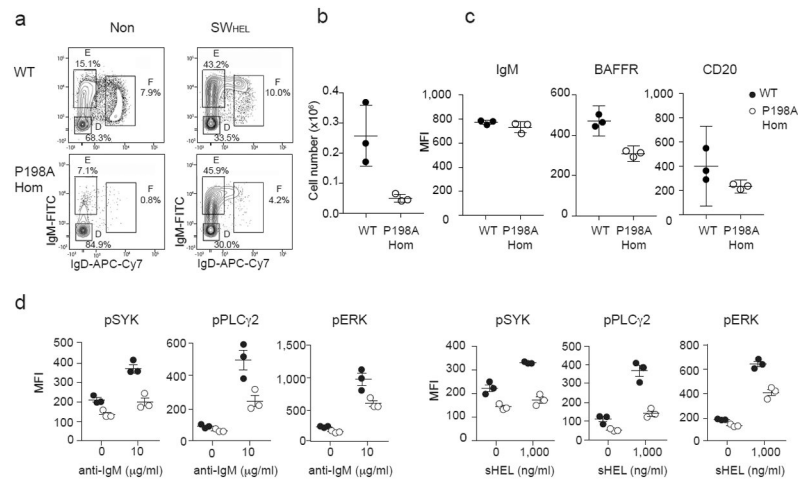
Figure 7. Impaired ZIP7 function results in reduced BCR signalling.
(**a**) Representative flow cytometry analysis of BM from WT (upper) and P198A-Hom (lower) mice, with (right) and without (left) co-expression of the SW$_{HEL}$ heavy and light chain transgenes. (**b**) Total numbers and (**c**) Mean fluorescence intensity (MFI) of surface IgM, BAFFR and CD20 on HEL binding cells from FrE in the BM of lethally irradiated CD45.1 mice reconstituted for 8 weeks with whole BM from CD45.2 WT (open circles) or P198A-Hom (closed circles) SW$_{HEL}$ mice, gated on B220$^+$CD24$^+$CD21$^-$HEL$^+$IgD$^-$ cells; n=3 mice per genotype; representative of 6 independent experiments. (**d**) Mean phospho-specific antibody binding to indicated intracellular signalling molecules downstream of the BCR, 5 min after stimulation of whole BM from WT/ SW$_{HEL}$ (closed circles) and P198A-Hom/ SW$_{HEL}$ (open circles) mice with media alone or 10μg/ml anti-IgM (two experiments) or 1,000ng/ml soluble Hen Egg Lysozyme (sHEL) and gated for Fr E as in **a**. In this figure, circles represent values from individual mice (n=3 per genotype), bars are means of groups and 95% CI; representative of 4 individual experiments.
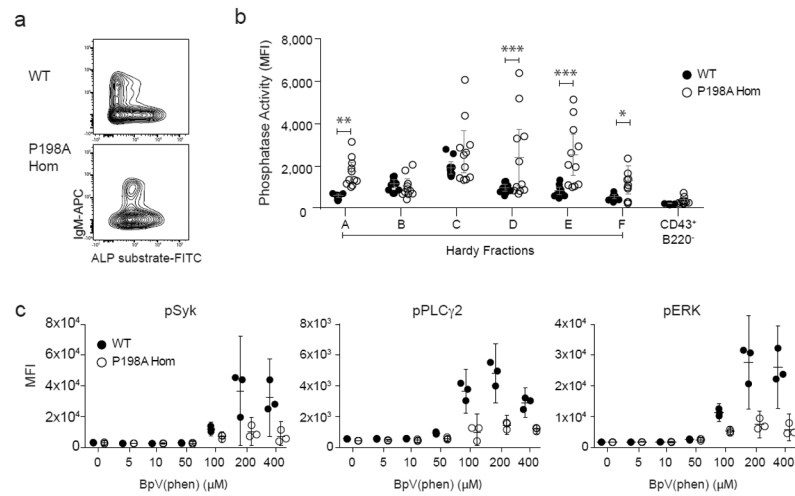
Figure 8. ZIP7-dependent inhibition of B cell phosphatase activity

(**a**) Representative flow cytometric staining of B220^{+}CD43^{−}IgD^{−} B cells from WT (upper) and P198A-Hom (lower) BM, showing phosphatase activity in the pre- (IgM^{−}) to immature (IgM^{+}) B cell transition; plots representative of 3 separate experiments, with n=4 mice per genotype in each experiment. (**b**) Mean phosphatase activity in B cell Hardy Fractions A-F and myeloid cells (B220^{−}CD43^{+}), from WT (closed circles) and P198A-Hom (open circles) BM. Results are pooled from 3 independent experiments, for a total of 11 mice per group, with comparison by two-way ANOVA (F 5.158; DF 6); *p=0.0438; **p=0.0010; ***p<0.0001. (**c**) Mean phospho-specific antibody binding to indicated intracellular signalling molecules downstream of the BCR, 30 min after treatment of WT (closed circles) and P198A-Hom (open circles) BM cells with the PTEN specific inhibitor BpV(phen), in the absence of BCR stimulation; gated on B220^{+}CD24^{+}CD21^{−}HEL^{+}IgD^{−} SW$_{HEL}$ transgenic B cells. In this figure, circles represent values from individual mice (n=3 per genotype), bars are means of groups and 95% CI. Data are representative of 4 independent experiments.

Table 1:

Laboratory parameters of humoral immunity in 6 patients with ZIP7 deficiency.

Quoted immunoglobulin (Ig) values were obtained within one month of presentation except in P3 (age 4 years), P4 (5 years) and P5 (2 years); B cells were measured at various ages ranging from 1 day (P2) to 14 years (P3).

Patient	P1	P2	P3	P4	P5	P6
ZIP7 variant 1	P190A	P190A	L217P	E451X	T395I	P190A
ZIP7 variant 2	E363K	E363K	Q372X	G458A	T395I	L217P
age (months) at presentation	<1	<1	12	23	<1	26
IgG (g/L)	1.0	*30.1	0.14	*4.58	<1.4	<1.7
IgA (g/L)	0.25	0.16	<0.06	<0.06	**0.17	<0.07
IgM (g/L)	<0.22	**0.19	<0.04	<0.04	**0.23	0.09
B cell (%)	<0.01	<0.01	<0.01	<0.02	<0.01	<0.01

*
value obtained after Ig supplementation

**
declining to undetectable